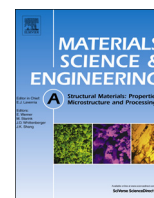




ELSEVIER

Contents lists available at ScienceDirect

Materials Science & Engineering A

journal homepage: www.elsevier.com/locate/msea

Evolution of microstructure and hardness in AZ31 alloy processed by high pressure torsion

Jitka Stráská^a, Miloš Janeček^a, Jenő Gubicza^{b,*}, Tomáš Krajňák^a, Eun Yoo Yoon^c, Hyoung Seop Kim^d

^a Department of Physics, Faculty of Mathematics and Physics, Charles University, Ke Karlovu 5, Prague 121 16, Czech Republic

^b Department of Materials Physics, Eötvös Loránd University, P.O.B. 32, Budapest H-1518, Hungary

^c Materials Deformation Department, Korea Institute of Materials Science, Changwon 642-831, South Korea

^d Department of Materials Science and Engineering, POSTECH, Pohang 790-784, South Korea

ARTICLE INFO

Article history:

Received 29 September 2014

Received in revised form

27 November 2014

Accepted 2 December 2014

Available online 10 December 2014

Keywords:

Magnesium alloys

High pressure torsion

Dislocations

Grain refinement

Hardness

ABSTRACT

A commercial MgAlZn alloy (AZ31) was processed by high pressure torsion (HPT) at room temperature, resulting in an extreme microstructure refinement down to the grain size of 150–250 nm. The microstructure evolution during HPT was investigated by transmission electron microscopy and X-ray diffraction line profile analysis. The microhardness was measured as a function of the distance from the center of the disk and the number of HPT revolutions. The detailed analysis of dislocation contrast factors in X-ray diffraction line profiles enables to determine the population of the different slip systems as a function of the imposed strain. The influence of microstructure and defect structure evolution on microhardness is discussed in detail.

© 2014 Elsevier B.V. All rights reserved.

1. Introduction

Magnesium-based alloys are very light constructional materials, but they have a few limitations such as low ductility, poor creep and corrosion resistance. However, mechanical and some other important properties determining the application of Mg alloys may be improved by refining the grain size to submicrometer or even nanometer level. A variety of special techniques can be used for the production of bulk ultrafine-grained (UFG) materials, e.g. equal channel angular pressing (ECAP) [1], high pressure torsion (HPT) [2], accumulative roll-bonding (ARB) [3], twist extrusion [4], multi-directional forging [5], etc. Among these techniques, which introduce the severe plastic deformation (SPD) in the material, the HPT is a very efficient method of grain refinement for many metals and alloys [6]. HPT was also successfully applied for producing consolidated materials from metal powders [7]. One significant advantage of the HPT method in the processing of magnesium alloys is that the grain refinement can be achieved at room temperature, since the high pressure inhibits the early failure of specimen [8]. It has also been shown that the evolution of microstructure and hardness in magnesium alloys during HPT can be tailored by varying the homologous temperature of processing and the alloying element content [9–12].

Due to an inhomogeneous strain introduced into the specimen by torsional straining in HPT an inhomogeneous microstructural refinement occurs. As a consequence the average grain size and mechanical properties vary along the radius of the disks. It was shown that the inhomogeneity of microstructure is reduced by increasing number of rotations [13]. After approximately 5 or more rotations (depending strongly on material) almost homogeneous microhardness distribution was observed by several authors [8,13,14].

It is well known that severe plastic deformation introduces a high density of dislocations and other lattice defects to the material. Dislocation structure and its evolution with strain influence the mechanical properties, microstructure refinement and grain fragmentation. It is therefore important to determine the variations of dislocation density and other lattice defects occurring during processing of the material by the SPD techniques and relate them with concurrent changes in the microstructure. The objective of this paper is to investigate the defect structure evolution in the AZ31 magnesium alloy after various strengthening levels caused by HPT and to correlate it to the microstructure and hardness evolution.

2. Experimental material and procedures

2.1. Material preparation

A commercial AZ31 alloy with a nominal composition of Mg–3% Al–1%Zn in the initial as cast state was used in this investigation.

* Corresponding author. Tel.: +36 1 3722876; fax: +36 1 3722811.

E-mail address: jeno.gubicza@ttk.elte.hu (J. Gubicza).

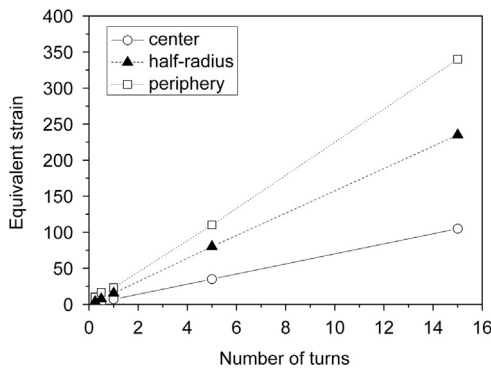


Fig. 1. The equivalent strain in the center, half-radius and periphery as a function of HPT turns.

Prior to HPT, the alloy was homogenized at 390 °C for 12 h. After homogenization the disk specimens with a diameter of 19 mm and thickness of 1–2 mm were cut from the billet. These specimens were processed by quasi-constrained HPT [15,16] at room temperature for $\frac{1}{4}$, $\frac{1}{2}$, 1, 3, 5 and 15 rotations. One more set of the samples was only pressed in the HPT device (marked $N=0$). The pressure of 2.5 GPa was applied and the anvil rotated with the speed of 0.1 rad/s. In order to facilitate the comparison between the microstructure evolution in the different locations of the specimens, the equivalent strain in the center, half-radius and periphery is given as a function of HPT turns in Fig. 1. The strain was calculated using finite element modeling and taking into account the shear strain, the compression and the outflow of the material (which results in thickness reduction). The details of this calculation can be found in Ref. [14].

2.2. Microhardness measurements

Vickers microhardness HV0.1 (with the applied load of 0.1 kg and holding time of 10 s) was measured on a semi-automatic Wolpert tester allowing automatic indentation. The regular square network of indents with the step of 0.5 mm was performed in one quarter of each specimen after HPT. In order to find the exact center of the specimen two additional lines of indents on the other half of the specimen were also done. Using this procedure the center of each specimen was found with the accuracy of ± 0.25 mm (assuming that the center has the minimum hardness). Data for the whole specimen were constructed from measured values symmetrically with respect to the center (data at the same distance from the center). The hardness values were measured twice and the average values were calculated. However, such “completed data” are not suitable for 3D-depicting. A smoothing procedure was applied to remove each wrongly indented or evaluated datum (a detailed description can be found in our previous paper [17]).

2.3. Microstructure investigation by electron microscopy

The microstructure evolution during HPT was investigated using a transmission electron microscope (TEM) Jeol 2000FX operated at 200 kV. Electron backscatter diffraction (EBSD) was performed with a FEI Quanta 200 FX scanning electron microscope equipped with EDAX EBSD camera and OIM software. All specimens for microstructure investigations were ground, mechanically polished and finally gently thinned by argon ions using Gatan PIPS ion mill at 4 kV.

2.4. Microstructure investigation by X-ray diffraction line profile analysis

The microstructure of the HPT-processed AZ31 samples was also studied by X-ray line profile analysis (XPLA). The X-ray line profiles were measured by a high-resolution diffractometer with $\text{CuK}\alpha_1$ radiation (wavelength: $\lambda=0.15406$ nm). The size of the X-ray beam spot on the sample surface was about 2×0.2 mm², where the longer dimension of the rectangular spot was set to be perpendicular to the disk diameter. XPLA measurements were carried out near the center and at the periphery of the disks. Due to the 2 mm high beam spot the parameters obtained at the center characterize an averaged microstructure between the center and 10% of the disk radius. The line profiles were evaluated by the Convolutional Multiple Whole Profile (CMWP) fitting method [18]. In this procedure, the diffraction pattern is fitted by the sum of a background spline and the convolution of the instrumental pattern and the theoretical line profiles related to the crystallite size and dislocations. The theoretical profile functions used in this fitting procedure are calculated on the basis of a model of the microstructure, where the crystallites have a spherical shape and log-normal size distribution. As an example, the fitting for the near center of the disk processed by $\frac{1}{2}$ HPT turn is shown in Fig. 2. The open circles and the solid line represent the measured data and the fitted curve, respectively.

The area-weighted mean crystallite size ($\langle x \rangle_{area}$), the dislocation density (ρ), the dislocation arrangement parameter (M), and parameters q_1 and q_2 depending on the population of the different slip systems were determined by the line profile analysis. The area-weighted mean crystallite size was calculated from the median and the variance, m and σ , of the log-normal size distribution as $\langle x \rangle_{area} = m \exp(2.5\sigma^2)$ [18]. The relative fractions of different dislocation slip systems were determined by comparing the theoretical dislocation contrast factors with the experimental values using the procedure described in [19].

In hexagonal materials there are 11 dislocation slip systems [20]. The dislocation contrast factor C_{hkl} characterizes the effect of a dislocation type on the broadening of X-ray peak with the indices hkl . For hexagonal polycrystalline materials the average contrast factors \bar{C}_{hkl} can be written in the following form [21]:

$$\bar{C}_{hkl} = \bar{C}_{hk0} (1 + q_1 z + q_2 z^2), \quad (1)$$

where q_1 and q_2 are two parameters depending on the anisotropic elastic constants of the crystal and the type of dislocation slip system. $z = (2/3)(l/ga)^2$, where a is the lattice constant in the basal

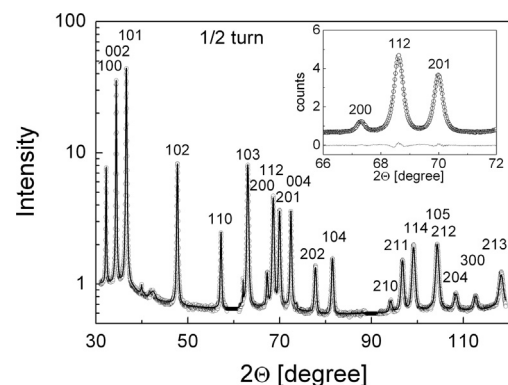


Fig. 2. The CMWP fitting for the near center of the disk processed by $\frac{1}{2}$ HPT turn. The open circles and the solid line represent the measured data and the fitted curve, respectively. The intensity is plotted in logarithmic scale. The inset shows a part of the diffractogram with a larger magnification. In the inset the intensity is plotted in linear scale and the difference between the measured and the fitted patterns is shown at the bottom.

plane and g is the magnitude of the diffraction vector. \bar{C}_{hko} is the average dislocation contrast factor for reflections $hk0$. The theoretical values of \bar{C}_{hko} , q_1 and q_2 for the 11 possible slip systems in the most common hexagonal materials have been calculated according to [22] and are listed in [21]. Each of the 11 slip systems has different theoretical values of \bar{C}_{hko} , q_1 and q_2 parameters, therefore the evaluation of the experimental values of q_1 and q_2 enables the determination of the prevailing dislocation slip systems in the specimen. The 11 dislocation slip systems can be classified into three groups based on their Burgers vectors: $b_1 = \frac{1}{3}\langle\bar{2}110\rangle$ ($\langle a \rangle$ type), $b_2 = \langle 0001 \rangle$ ($\langle c \rangle$ type) and $b_3 = \frac{1}{3}\langle\bar{2}113\rangle$ ($\langle c+a \rangle$ type). There are 4, 2 and 5 slip systems in the $\langle a \rangle$, $\langle c \rangle$ and $\langle c+a \rangle$ Burgers vector groups, respectively. A computer program was elaborated in order to determine the distribution of dislocations among the different slip systems from the measured values of q_1^m and q_2^m [20]. In this procedure those dislocation populations are determined which yield the same hkl dependence of line broadening as obtained from the experiment. In the case of dislocations the mean-square-strain, which determines the peak breadth, can be expressed as [23]:

$$\langle \varepsilon_{g,L}^2 \rangle \cong \frac{\rho \bar{C}_{hkl} b^2}{4\pi} f(\eta), \quad (2)$$

where

$$\eta = \frac{1}{2} \exp\left(-\frac{1}{4}\right) \frac{L}{R_e^*}, \quad (3)$$

and ρ , b and R_e^* are the density, the modulus of Burgers vector and the effective outer cut-off radius of dislocations, respectively. The function $f(\eta)$ is referred to as Wilkens function and given in [23]. Eq. (2) shows that the variation of line broadening with the orientation of diffraction vector is determined by \bar{C}_{hkl} . Setting the experimental value of $\bar{C}_{hkl} b^2$ equal to the theoretical value calculated by averaging for the 11 slip systems, the following equation is obtained:

$$\bar{C}_{hko}^m (1 + q_1^m z + q_2^m z^2) b_m^2 = \sum_{i=1}^{11} f_i \bar{C}_{hko}^i (1 + q_1^i z + q_2^i z^2) b_i^2, \quad (4)$$

where letter “ m ” indicates the values obtained from the measured profile, “ i ” denotes the theoretical values calculated for the i th slip system and f_i is the fraction of dislocations in the i th slip system. The polynomials in the two sides of Eq. (4) give the same values, if the coefficients of the terms with the same degrees are equal. This condition yields the following equations:

$$q_1^m = \frac{\sum_{i=1}^{11} f_i \bar{C}_{hko}^i b_i^2 q_1^i}{\sum_{i=1}^{11} f_i \bar{C}_{hko}^i b_i^2}, \quad q_2^m = \frac{\sum_{i=1}^{11} f_i \bar{C}_{hko}^i b_i^2 q_2^i}{\sum_{i=1}^{11} f_i \bar{C}_{hko}^i b_i^2}, \quad \sum_{i=1}^{11} f_i = 1. \quad (5)$$

There is no equation for \bar{C}_{hko}^m since it is not an independent parameter in the evaluation of line profiles as \bar{C}_{hko}^m is multiplied by the dislocation density in Eq. (2). The 11 values of f_i cannot be determined from the three formulas in Eq. (5), therefore additional restrictions are made for f_i . It is assumed that in each Burgers vector group the non-zero fractions are equal. This assumption reduces the number of variables to three, which are denoted by f_a , f_c and f_{c+a} . The computer program written for the evaluation of Burgers vector population in hexagonal materials (referred to as *Hexburger* [20]) first selects some slip systems from $\langle a \rangle$ dislocation group and for these slip systems the weights are f_a . For other slip systems in this group the weights are zero. This procedure is also carried out for $\langle c \rangle$ and $\langle c+a \rangle$ Burgers vector groups where the non-zero weights are f_c and f_{c+a} , respectively. Inserting the theoretical values of \bar{C}_{hko}^i , b_i , q_1^i and q_2^i into Eq. (5), the values of f_a , f_c and f_{c+a} are determined. If these fractions have positive values the program stores them as one of the possible solutions. The number of the

possible selections from the dislocation slip systems equals $(2^4 - 1)(2^2 - 1)(2^5 - 1) = 1395$. Finally, the positive solutions for the weights can be averaged for each slip system, leading to the fractions of the 11 dislocation types. The fractions of the three Burgers vector groups, f_a , f_c and f_{c+a} , are obtained by the summation of the fractions of the related slip systems. It should be noted that the *Hexburger* software gives directly the solutions for f_a , f_c and f_{c+a} in a file for each selection of slip systems. Then, f_a , f_c and f_{c+a} can be determined by dividing f_a , f_c and f_{c+a} with the number of slip systems with non-zero weights in $\langle a \rangle$, $\langle c \rangle$ and $\langle c+a \rangle$ Burgers vector groups, respectively. In practice, the line profile evaluation directly yields $\rho b^2 \bar{C}_{hko}^m$, q_1^m and q_2^m . In the CMWP fitting procedure a preliminary value for $b^2 \bar{C}_{hko}^m$ is assumed and the evaluation gives a first approximation for ρ , since its value depends on $\rho b^2 \bar{C}_{hko}^m$. Then, the Burgers vector population should be determined by the above described method. Using the fractions of 11 slip systems as weights, the real average value of $\rho b^2 \bar{C}_{hko}^m$ can be determined. Finally, this parameter is used for obtaining the exact value of the dislocation density. It is noted that dislocations with large Burgers vectors ($\langle c \rangle$ and $\langle c+a \rangle$ dislocations) are difficult to form due to their high energies. However, these dislocations should be incorporated into the Burgers vector population analysis as besides twinning only $\langle c \rangle$ and $\langle c+a \rangle$ dislocations can result in plastic strain in the crystallographic c -direction in the grains of hexagonal polycrystalline materials. It should also be noted that for Mg the contrast factors of prismatic edge (PrE) and pyramidal edge (PyE) dislocations in the $\langle a \rangle$ -type slip system family are close to each other [19]. Therefore, it is difficult to distinguish between them and usually they receive nearly equal populations in the analysis.

3. Results and discussion

3.1. Microhardness

Microhardness variations across the surface of individual specimens after different number of HPT turns are shown in Fig. 3. These 3D plots show clearly that HPT straining introduces an inhomogeneity in the material which is manifested by the minimum value of the hardness in the near center and much higher microhardness values in the specimen periphery. Fig. 4 shows the average microhardness as a function of the distance from the center. This inhomogeneous microhardness distribution is formed already in the specimen after 1/4 HPT turn where the central region exhibits the average value of $Hv \approx 80$ –85 while near the periphery the Hv varies between 110 and 115. Note, that HPT straining is very efficient in material strengthening, as already after $N=1/4$ the microhardness increased by ~ 25 MPa and ~ 50 MPa in the near center and the periphery of the specimen, respectively, as compared to the material which was only pressed in the HPT anvil ($N=0$), cf. Fig. 3a and b. For $N=0$ the hardness in the near center was 60 and increased to 85 in the periphery. The enhanced microhardness observed in peripheral regions of this specimen is caused by the material outflow due to pressing and the consequent strengthening [2]. With the increasing number of HPT turns the microhardness is continuously smoothed and in the specimen after 15 turns ($N=15$) almost homogenous distribution of microhardness was measured. The detailed inspection of 3D plots in Fig. 3 reveals the undulating character of microhardness variations and the development of deformation in the material which is consistent with the model of strain gradient plasticity [24]. For low stacking fault energy materials such as AZ31 alloys ($\gamma=27.8$ mJ/m² in the basal plane [25]) this model predicts a two-stage development of microhardness undergoing inhomogeneous straining. Initially, in early stages of HPT

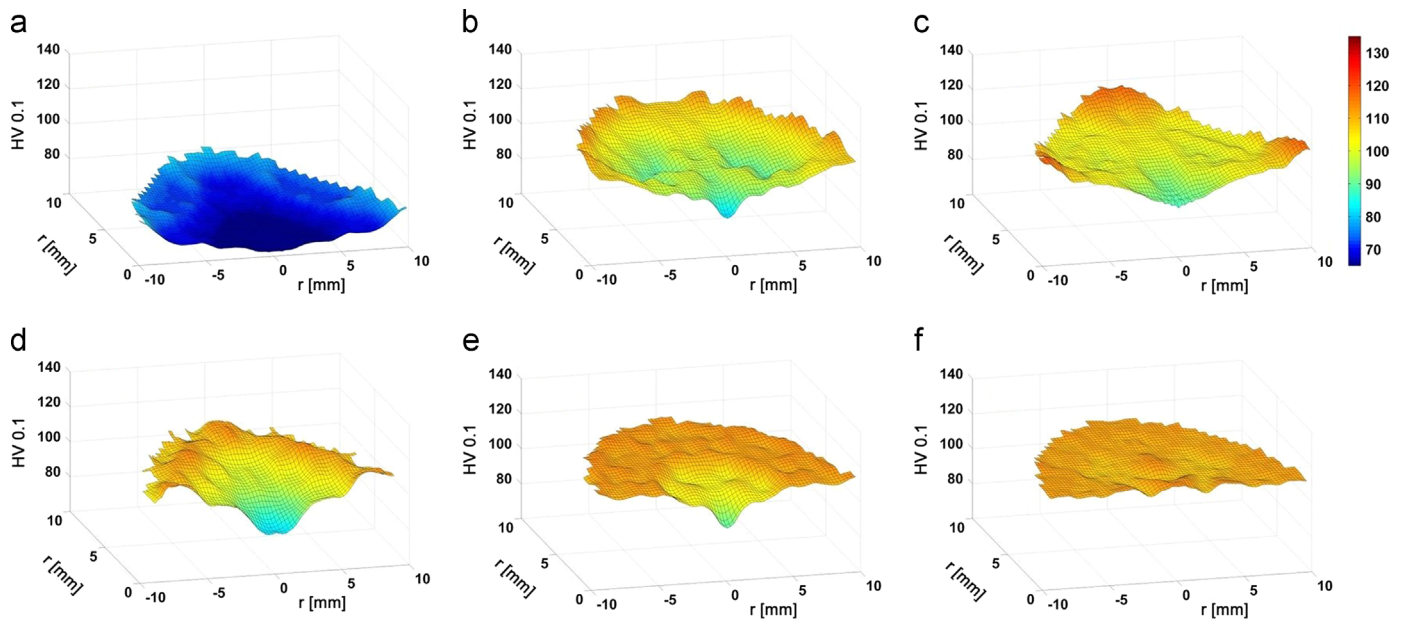


Fig. 3. 3-D plots of microhardness distribution on the surface of specimens after different number of HPT turns N ((a) $N=0$, (b) $N=1/4$, (c) $N=1/2$, (d) $N=1$, (e) $N=5$ and (f) $N=15$).

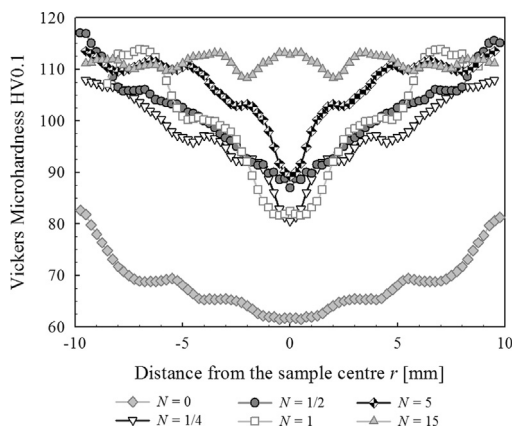


Fig. 4. The average microhardness as a function of the distance from the center.

straining, the microhardness distribution is characterized by low values in the near center and much higher values in regions close to the periphery. With increasing strain introduced to the material by HPT processing the microhardness tends to saturate by continuous extending of the region of high microhardness from the specimen periphery towards its center.

3.2. Microstructure observations by electron microscopy

Due to the inhomogeneous character of the strain imposed in HPT-processing, the microstructure evolution was investigated by TEM in both near center and periphery. It should be noted that the position of the microstructures in the center has an uncertainty of about ± 0.25 mm. The TEM micrographs in Fig. 5 show the microstructure in the near center of HPT specimens. In Fig. 5a the microstructure of the specimen after 1 turn is shown. It is seen that the grain fragmentation has already started. The microstructure consists of bands of elongated subgrains of the average width of 300–400 nm. However, the microstructure of this specimen is rather inhomogeneous. In other zones (not shown here), the typical heavily deformed structure with no subgrain/grain formation comprising only large stress fields was observed. Note, that the average grain size of the as cast material was approximately 150–200 μm [26].

Extensive grain refinement is first observed in the near center after 5 HPT, see Fig. 5b, where fine grains with the size of 200–300 nm are clearly seen. The microstructure of this specimen remains inhomogeneous. In some zones bands of elongated subgrains similar to those in Fig. 5a were also observed. Homogeneous microstructure containing fine grains with the average size of 150–200 nm was observed only in the specimen after 15 HPT turns. An example of such microstructure is shown in Fig. 5c where newly formed grains with almost no dislocations and high angle boundaries are clearly seen (grain misorientation was also inspected by electron diffraction). The inhomogeneous character of microstructure throughout the disk specimen is clearly seen by the inspection of Fig. 6 which displays the microstructure evolution in the periphery of individual specimens. Grain fragmentation and the formation of elongated bands of subgrains occurred already during early stages of HPT straining, see the TEM micrograph of the specimen $N=1/4$ in Fig. 6a. In the specimen after 1 turn (Fig. 6b) fine grains are already formed and their size ranges between 150 and 250 nm. Further HPT straining results in slight grain fragmentation only without significant microstructure changes, cf. Fig. 6b–d.

If the correlation between microhardness and grains size according to Hall–Petch relation is inspected one can see the good agreement in the following three cases. First, significantly higher values of microhardness in the periphery of specimens as compared to their near centers (up to $N=5$) agrees well with the grain structure in the individual specimens. In all these specimens the grains in the near centers are either not fragmented, i.e. remain coarse or are significantly coarser than in peripheral regions, cf. Figs. 5 and 6. Only in the specimens after 15 turns the grain structures in the near center and in the periphery are almost the same which is reflected by homogeneous microhardness values throughout the specimen. Secondly, continuously increasing values of microhardness in the near center of the specimens with increasing number of turns corresponds well to the grain fragmentation and refinement in the respective specimens, cf. Fig. 5a–c. Thirdly, the small microstructure changes in the specimen periphery for $N > 1$ reflect well the slight microhardness variations in these specimens, cf. Fig. 6b–d.

Our previous investigation of microstructure evolution by TEM in AZ31 alloy processed by another widely used technique of SPD, namely equal channel angular pressing (ECAP) [26] allows us to

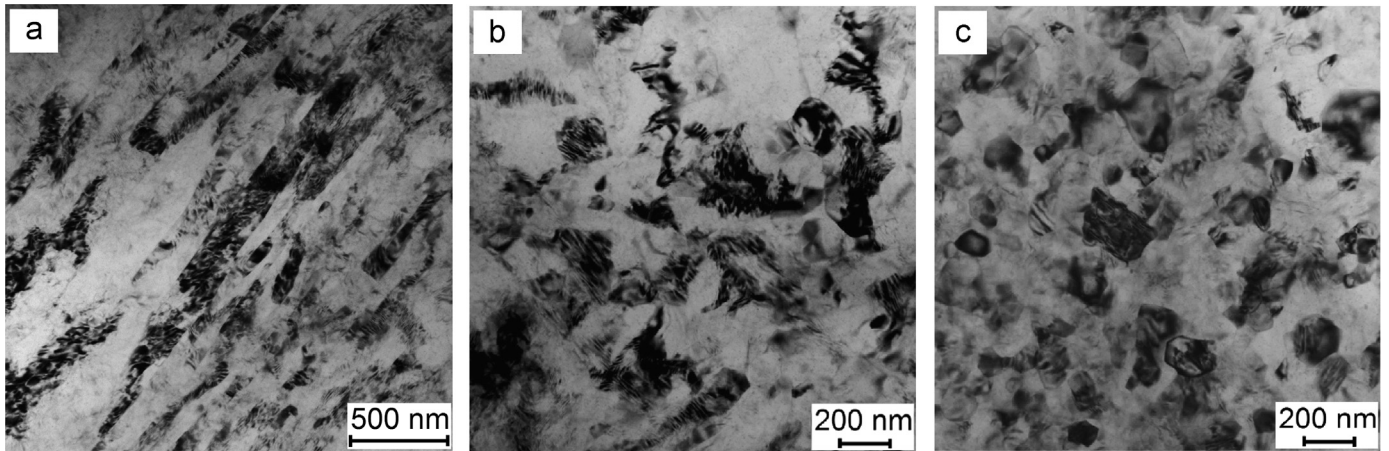


Fig. 5. TEM micrographs showing the evolution of microstructure in the near center of specimens after different number of HPT turns N ((a) $N=1$, (b) $N=5$ and (c) $N=15$).

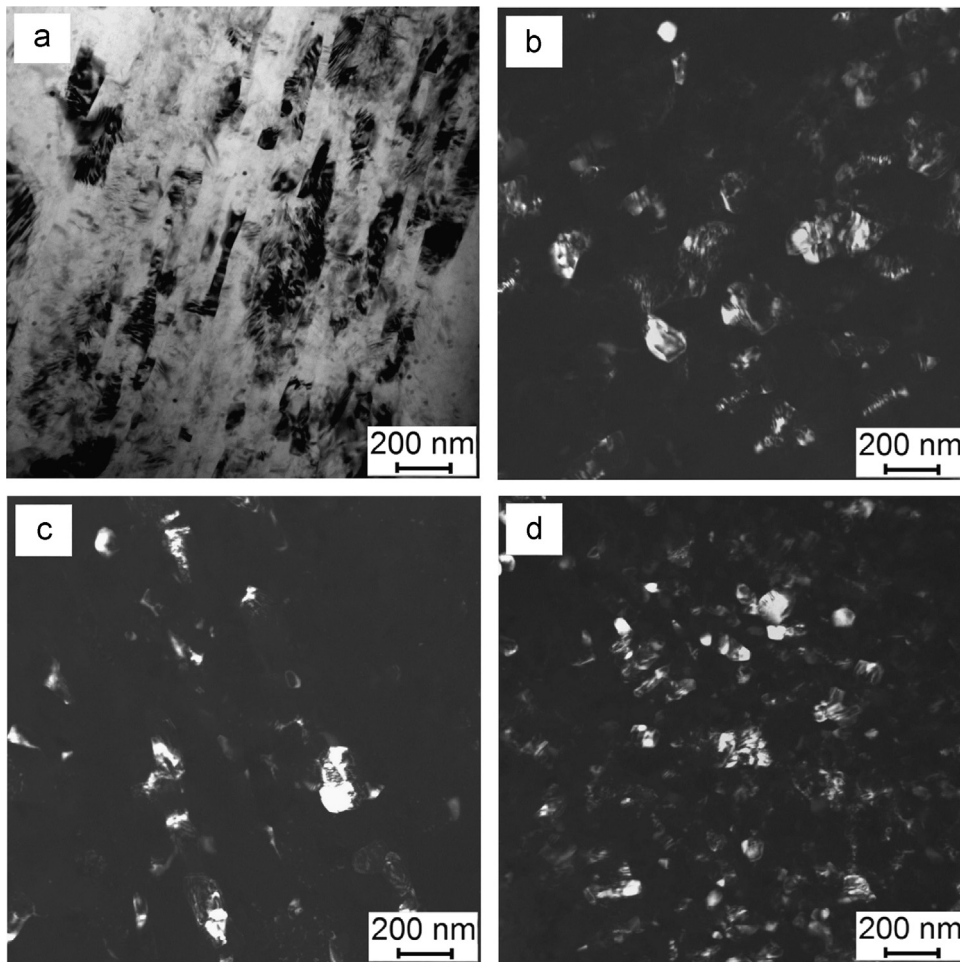


Fig. 6. TEM micrographs showing the evolution of microstructure near the edge of specimens after different number of HPT turns N ((a) $N=1/4$, (b) $N=1$, (c) $N=5$ and (d) $N=15$).

compare the effectiveness of these two techniques in grain refinement. The average grain size in AZ31 alloy processed by 12 passes of ECAP using route B_c was approximately 500 nm which is almost 5 times larger than the value observed in the material after 15 turns of HPT. Therefore the effectiveness of HPT in grain refinement is significantly higher than that of ECAP. The possible reasons of this difference are the pressure, the strain and the temperature of material processing. The high pressure applied during HPT allows

us to process the material at room temperature while in ECAP-processing the specimens had to be pressed at high temperature of approximately 180 °C. Therefore, the recrystallization and other related phenomena resulting in grain coarsening during material processing are obviously more effective in the case of high-temperature ECAP than for room-temperature HPT.

EBSD observations were also performed in selected specimens after HPT. The experiments were done in the disk center and at the

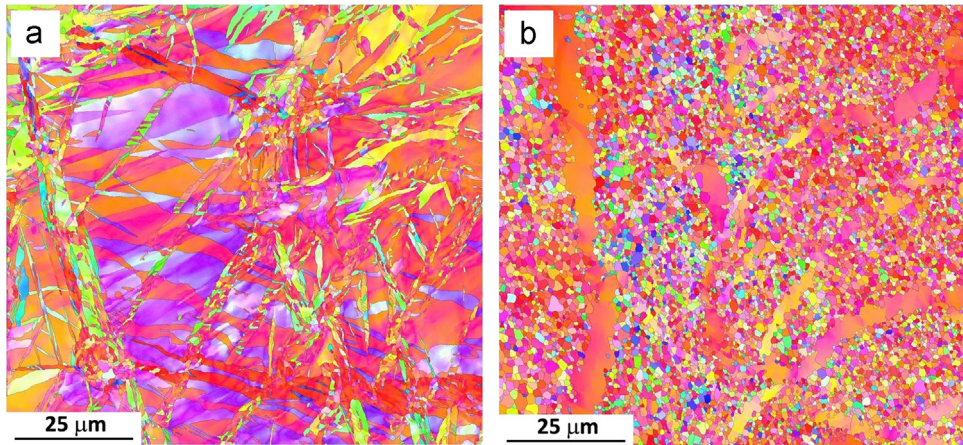


Fig. 7. IPF image of grain structure in the specimen after 1 HPT turn: (a) near center and (b) at the half-radius.

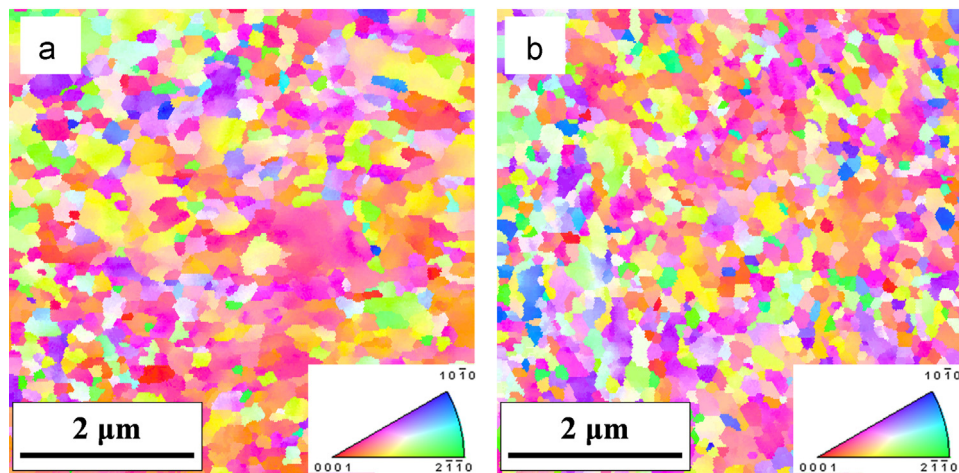


Fig. 8. IPF maps obtained from ACOM-TEM investigations performed at the periphery for 1 (a) and 15 (b) turns.

half-radius, i.e. 5 mm from the center. The very fine grain structure near specimen periphery did not allow EBSD observation. In Fig. 7 one example for EBSD map is given just to present a more global image of microstructure inhomogeneity in HPT specimens than that observed by TEM. Fig. 7a displays the initial stages of grain fragmentation in zones around the specimen center deformed by 1 turn of HPT. The initial coarse grains are already divided by several families of elongated subgrains similar to those observed by TEM, cf. Fig. 5a. The rests of the original grains are also clearly seen in several parts of the specimen (also observed by TEM). The zone at the half-radius of the same specimen is shown in Fig. 7b. Due to significantly higher strain as compared to the near center, the grain fragmentation is well developed in this zone. The grain structure has bimodal nature which contains several elongated coarse grains with the length of about $100\ \mu\text{m}$ and the width of about $10\ \mu\text{m}$, while the majority of grains are equiaxed with the average size of approximately $150\text{--}200\ \text{nm}$. Most of these fine grains have their crystallographic c -axes perpendicular to the specimen surface. The development of bimodal microstructure can be explained by the grain refinement mechanism in hexagonal materials. It has been shown that above a critical initial coarse grain size (which is about $10\ \mu\text{m}$), the grain refinement starts with the development of an inhomogeneous grain structure [27,28]. The new grains form along the boundaries of the initial coarse grains in a necklace-like arrangement. As a consequence, if the initial grain size is large enough, the fine grains at the grain boundaries and the internal volumes of the initial coarse grains

give a bimodal grain structure. The microstructure in the peripheral zones was investigated by automated crystallographic orientation mapping in TEM (ACOM-TEM). As an example, ACOM-TEM images taken at the periphery for 1 and 15 turns are shown in Fig. 8a and b, respectively. The average grain size at the edge of the disk after 1 turn is about $250\ \text{nm}$ which is only slightly larger than the value determined in the sample processed by 15 turns ($\sim 200\ \text{nm}$). This observation is in accordance with the similar hardness values at the periphery of these samples and indicates an early saturation of the microstructure at the edge of the HPT disk. Strong texture was not observed in the ACOM-TEM images either after 1 or 15 turns.

3.3. X-ray line profile analysis

The evolution of the crystallite size and the dislocation structure during HPT-processing were investigated by XLP. The area-weighted mean crystallite size and the dislocation density at the near center and the periphery of the disks for different number of HPT turns are listed in Table 1. The evolution of the crystallite size and the dislocation density as a function of HPT turns are plotted in Figs. 9 and 10, respectively. There is a significant density of dislocations ($\sim 3 \times 10^{14}\ \text{m}^{-2}$) even in the initial sample which was subjected to a pressure of $2.5\ \text{GPa}$ in the HPT facility without rotation (0 turn). The dislocation density increased twice while the crystallite size considerably decreased due to HPT. However, the crystallite size and the parameters of the dislocation structure

Table 1

The area-weighted mean crystallite size ($\langle x \rangle_{area}$) and the dislocation density (ρ) at the center and the periphery of the disks for different number of HPT turns.

Number of turns	$\langle x \rangle_{area}$ [nm]	ρ [10^{14} m^{-2}]
<i>Center</i>		
0	531 ± 60	3 ± 0.3
1/4	87 ± 9	5.4 ± 0.6
1/2	75 ± 8	7.8 ± 0.8
1	66 ± 7	6 ± 0.6
3	79 ± 9	5 ± 0.6
5	64 ± 7	5.6 ± 0.6
15	84 ± 9	5.5 ± 0.6
<i>Periphery</i>		
0	107 ± 12	3.6 ± 0.4
1/4	67 ± 7	6.7 ± 0.7
1/2	66 ± 7	6.7 ± 0.7
1	69 ± 8	6.6 ± 0.7
3	71 ± 8	6.3 ± 0.7
5	70 ± 8	6.1 ± 0.7
15	62 ± 7	6.1 ± 0.7

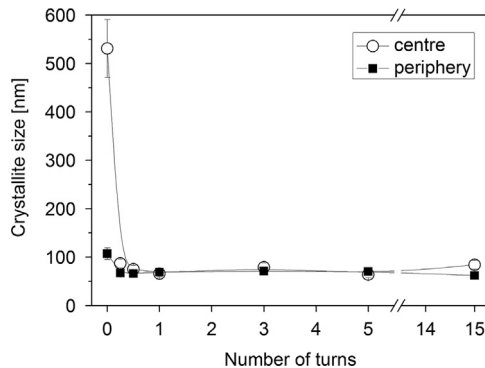


Fig. 9. The average crystallite size versus the number of turns for the near center and the periphery of the HPT-processed disks.

saturated even after $\frac{1}{4}$ HPT turn and significant changes were not observed with increasing deformation up to 15 revolutions. The maximum dislocation density and minimum crystallite size were about $6 \times 10^{14} \text{ m}^{-2}$ and 70 nm, respectively. Additionally, considerable difference between the crystallite size and the dislocation structure at the near center and the periphery was not detected despite the various imposed strain values. These observations suggest an early saturation of the microstructural parameters with increasing strain during HPT-processing at room temperature. Note that the crystallite size obtained by XLPAs is much smaller than the grain size determined by TEM. This observation is in accordance with former studies and can be explained by the fact that the crystallite size usually corresponds to the subgrain size in severely deformed microstructures. Therefore, there is no correlation between the crystallite and grain sizes, but rather they complementarily describe the hierarchical nature of the microstructures obtained by SPD. Comparing TEM and XLPAs results, it can be concluded that the saturation of the subgrain size and the dislocation density occurred earlier than reaching the minimum grain size during HPT. Note that the saturation dislocation density and crystallite size in the present experiments were higher and lower, respectively, than the values obtained in EX-ECAP-processing at 180 °C ($1.4 \times 10^{14} \text{ m}^{-2}$ and 120 nm [26]). This can be explained by much lower temperature and higher pressure of HPT since both retard the annihilation of dislocations. Additionally, it has been shown that $\text{Mg}_{17}\text{Al}_{12}$ secondary phase was formed in

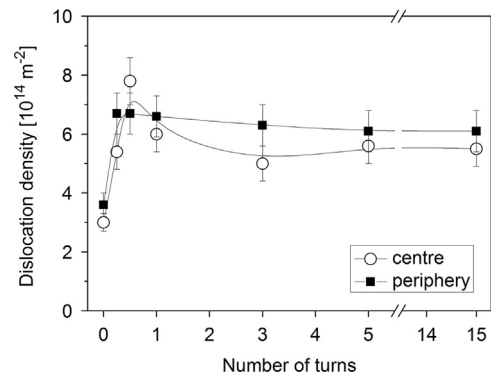


Fig. 10. The dislocation density versus the number of turns for the near center and the periphery of the HPT-processed disks.

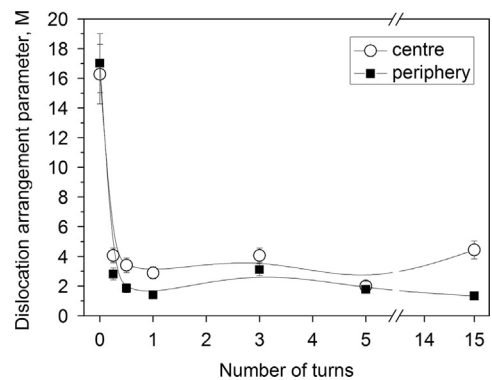


Fig. 11. The dislocation arrangement parameter M versus the number of turns for the near center and the periphery of the HPT-processed disks.

the Mg–3%Al–1%Zn alloy during ECAP at 180 °C while the Al and Zn alloying elements remained in solid solution during the present HPT experiments due to the low processing temperature [26]. The solute atoms have a pinning effect on dislocations, thereby contributing to the higher dislocation density in the HPT-processed specimen.

The dislocation arrangement parameter (M) as a function of the number of HPT turns is plotted in Fig. 11. The parameter M considerably decreased due to HPT-processing even after $\frac{1}{4}$ turn and did not change significantly with the increasing number of revolutions. The lower value of M indicates a more screened strain field of dislocations due their arrangement into low energy configurations, such as dipoles or low angle grain boundaries. The slightly lower M at the periphery indicates a more advanced stage in this process due to the larger imposed strain.

The analysis of the population of the different slip systems shows that the majority of dislocations have $\langle a \rangle$ -type Burgers-vector (60–80%) in both the initial (compressed) and HPT-processed states. This can be explained by their lowest formation energy due to their shortest Burgers-vector. The relative fraction of screw dislocations increased from $\sim 10\%$ (compressed state) to 30–40% due to HPT-straining. This observation can be attributed to the strong hindering effect of dislocation dissociation on the annihilation of screw dislocations [29]. In AZ31 alloy the dislocations are dissociated into partials due to the low stacking fault energy which impedes both cross-slip of screw dislocations and climb of edge dislocations. However, this effect is stronger for screw dislocations, as the characteristic time for cross-slip depends exponentially on the splitting distance while for climb of edge dislocations this function is only quadratic [29]. The more hindered annihilation of screw dislocations compared to that of edge ones resulted in an increase of the fraction of screw dislocations during HPT-straining.

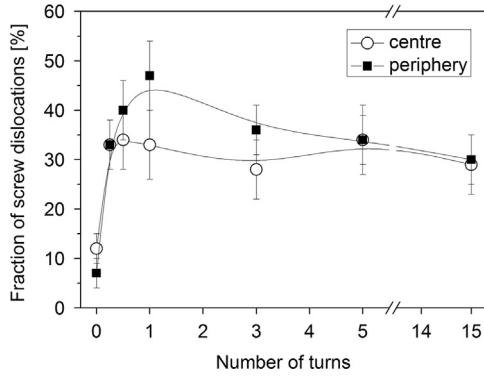


Fig. 12. The relative fraction of screw dislocations versus the number of turns for the near center and the periphery of the HPT-processed disks.

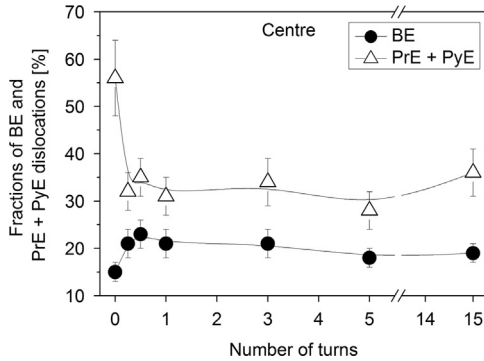


Fig. 13. The sum of the relative fractions of prismatic (PrE) and pyramidal (PyE) $\langle a \rangle$ -type edge dislocations and the fraction of basal (BE) dislocations versus the number of turns for the near center of the HPT-processed disks.

The evolution of the fraction of screw dislocations as a function of HPT turns is plotted in Fig. 12 for both the central and peripheral parts of the deformed disks. It should be noted that the fraction of screw dislocations saturated even at $\frac{1}{4}$ turn and significant difference between the values in the near center and the periphery was not observed, in accordance with the evolution of other parameters of the dislocation structure.

X-ray line profile analysis also revealed that the populations of the different slip systems for $\langle a \rangle$ -type edge dislocations also changed during HPT-processing. Namely, the sum of the fractions of prismatic (PrE) and pyramidal (PyE) edge dislocations decreased from about 55% to 30%, while the population of basal edge (BE) dislocations slightly increased from 15% to 20% in the near center of the disks, as shown in Fig. 13. A similar evolution of the dislocation fractions occurred in the periphery of the disks. This change in the dislocation population can be explained by the fact that in Mg with c/a lattice parameters ratio larger than 1.6 the slip occurs most easily in the basal plane at low temperatures [30]. Additionally, the stacking fault energy in the basal plane is smaller than in other slip planes [31], therefore there is a larger dissociation degree of basal dislocations which impedes their annihilation during straining, leading to an increase of their fraction after HPT.

3.4. The contribution of grain boundaries to strengthening

The combination of XPLA results and the microhardness measurement allows us to assess the role of grain boundaries in strengthening and to determine their contribution to the yield strength in different zones (center and periphery) of AZ31 specimens processed by HPT. The yield strength (σ) at the near center and the periphery of the individual specimens was estimated as one-third of the Vickers microhardness which was converted into

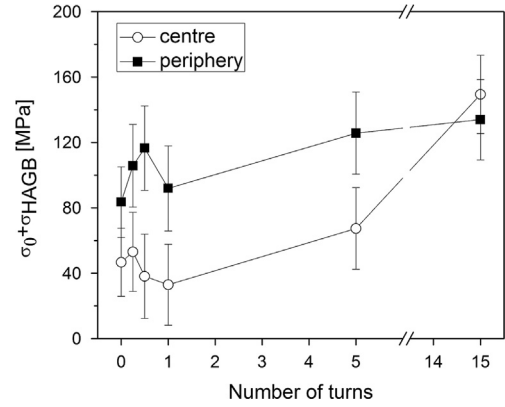


Fig. 14. The sum of the friction stress and the yield strength contribution of HAGBs as a function of the number of HPT turns.

MPa units by multiplying the Hv values with 9.81. We assume that the contributions of dislocations and high-angle grain boundaries (HAGBs) are added linearly, and the dislocation hardening is calculated according to the Taylor-formula as:

$$\sigma_D = \alpha M^T G b \rho^{1/2}, \quad (6)$$

where α is a constant (0.3 [32]), G is the shear modulus (17 GPa [33]), b is the average length of the Burgers vector calculated according to the fractions of the different slip systems, M^T is the Taylor factor (4.5 was selected for texture free Mg [32]). It is noted that the contribution of low-angle grain boundaries (LAGBs) to the strength is included in the Taylor-equation since these boundaries consist of dislocations. The sum of the friction stress (σ_0) and the strength caused by HAGBs (σ_{HAGB}) was determined as the difference between σ and σ_D , and plotted as a function of the number of HPT turns in Fig. 14. As σ_0 is constant for all numbers of turns, the change of $\sigma_0 + \sigma_{HAGB}$ with increasing number of turns reflects the variation of grain-boundary strengthening. It can be seen that in the near center the strength contribution of HAGBs (open circles) increased considerably only when the number of turns reached $N=5$. This result is in accordance with the significant grain refinement in specimen center for $N \geq 5$ as observed by TEM. On the other hand, the strength contribution of HAGBs in the specimen periphery increased even for $N=1/4$ and remained almost unchanged for larger numbers of turns (full squares). This is also in agreement with TEM observations as considerable grain refinement was observed in the disk periphery already after $\frac{1}{4}$ turn and the grain size was only slightly reduced during further HPT straining. It is noted that σ_{HAGB} involves the strengthening contribution of twin boundaries as they are special HAGBs. It should also be noted that the dislocation strengthening (160–260 MPa) is larger than the contribution of HAGBs (< 100 MPa) irrespective of the number of turns and the location along the disk radius. It is worth to notice that the conclusions obtained from the above analysis are independent of the selected addition rule for the dislocation and HAGB hardening contributions.

4. Conclusions

1. HPT straining at room temperature results in a strong grain refinement and introduces a lateral inhomogeneity of the microhardness and microstructure in AZ31 alloy. Significantly lower values of microhardness are observed in the near center than in its periphery. This microhardness inhomogeneity is continuously smeared out by extending the zone of enhanced microhardness from the specimen periphery towards its center. Lateral strain inhomogeneity imposed by HPT controls the

speed of grain fragmentation which is significantly higher in peripheral zones than in the near center resulting in much finer grains in the periphery than in the center. After a certain strain (15 HPT turns in our case) both the microhardness and the microstructure becomes homogeneous. Microhardness examinations correlate well with microstructure results.

2. There is a significant density of dislocations ($\sim 3 \times 10^{14} \text{ m}^{-2}$) even in the initial sample which was subjected to a pressure of 2.5 GPa in the HPT facility without rotation. The crystallite size decreased while the dislocation density increased during torsion by HPT. The crystallite size and the parameters of the dislocation structure reached their saturation values even at $\frac{1}{4}$ turn during HPT at room temperature. The maximum dislocation density and minimum crystallite size were about $6 \times 10^{14} \text{ m}^{-2}$ and 70 nm, respectively. Further increment in the number of HPT revolutions did not yield significant changes in the dislocation structure up to 15 turns. Additionally, considerable difference between the dislocation structures at the near center and the periphery of the HPT-processed disks was not observed, indicating an early saturation with the increasing imposed strain. It can be concluded that the dislocation density saturated earlier than the grain size, i.e. the grain refinement continued even after the dislocation density reached its maximum value.
3. The majority of dislocations have $\langle a \rangle$ -type Burgers-vector in both the initial (compressed) and HPT-processed states which can be explained by their lowest formation energy due to their shortest Burgers-vector. The relative fraction of screw dislocations was about 10% in the initial (compressed) state which increased up to 30–40% due to HPT straining. The sum of the fractions of $\langle a \rangle$ -type prismatic and pyramidal edge dislocations decreased while the population of basal dislocations increased during HPT-straining.
4. The dislocation strengthening was larger than the contribution of HAGBs irrespective of the number of turns and the location along the disk radius. HAGBs hardened the material considerably in the near center and the periphery only after 5 and $\frac{1}{4}$ turns, respectively. This result is in accordance with TEM observations which revealed an earlier grain refinement at the periphery in the HPT-processed disks.

Acknowledgments

This work was financially supported by Czech Science Foundation GACR under the Grant 14-36566G and student foundations GAUK 530712/2012 and SVV 2014-265303. J.G. acknowledges financial support by the Hungarian Scientific Research Fund, OTKA, Grant no. K-109021. The authors are grateful to Prof. Godet and Dr.

Galceran (Université Libre de Bruxelles) for ACOM-TEM investigations.

References

- [1] R.Z. Valiev, T.G. Langdon, *Prog. Mater. Sci.* 51 (2006) 881–898.
- [2] A.P. Zhilyaev, T.G. Langdon, *Prog. Mater. Sci.* 53 (2008) 893–979.
- [3] Y. Saito, H. Utsunomiya, N. Tsuji, T. Sakai, *Acta Mater.* 47 (1999) 579–583.
- [4] V.N. Varyutkhin, Y. Beygelzimer, S. Synkov, D. Orlov, *Mater. Sci. Forum* 503–504 (2006) 335–340.
- [5] X. Yang, Y. Okabe, H. Miura, T. Sakai, *J. Mater. Sci.* 47 (2012) 2823–2830.
- [6] Z. Horita, D.J. Smith, M. Furukawa, M. Nemoto, R.Z. Valiev, T.G. Langdon, *J. Mater. Res.* 11 (1996) 1880–1890.
- [7] E.Y. Yoon, D.J. Lee, T.S. Kim, H.J. Chae, P. Jenei, J. Gubicza, T. Ungár, M. Janeček, J. Vrátná, S. Lee, H.S. Kim, *J. Mater. Sci.* 47 (2012) 7117–7123.
- [8] T.G. Langdon, *Acta Mater.* 61 (2013) 7035–7059.
- [9] Y. Huang, R.B. Figueiredo, T. Baudin, F. Brisset, T.G. Langdon, *Adv. Eng. Mater.* 14 (2012) 1018–1026.
- [10] Y. Huang, R.B. Figueiredo, T. Baudin, A.L. Helbert, F. Brisset, T.G. Langdon, *J. Mater. Sci.* 47 (2012) 7796–7806.
- [11] A. Al-Zubaydi, R.B. Figueiredo, Y. Huang, T.G. Langdon, *J. Mater. Sci.* 48 (2013) 4661–4670.
- [12] M. Kawasaki, R.B. Figueiredo, Y. Huang, T.G. Langdon, *J. Mater. Sci.* 49 (2014) 6586–6596.
- [13] A.P. Zhilyaev, G.V. Nurislamova, B.K. Kim, M.D. Baro, J.A. Szpunar, T.G. Langdon, *Acta Mater.* 51 (2003) 753–765.
- [14] J. Vrátná, M. Janeček, J. Čížek, D.J. Lee, E.Y. Yoon, H.S. Kim, *J. Mater. Sci.* 48 (2013) 4705–4712.
- [15] A. Vorhauer, R. Pippan, *Scr. Mater.* 51 (2004) 921–925.
- [16] F. Wetscher, A. Vorhauer, R. Pippan, *Mater. Sci. Eng. A* 410–411 (2005) 213–216.
- [17] J. Vrátná, M. Janeček, J. Stráská, H.S. Kim, E.Y. Yoon, *Magnes. Technol.* 2011 (2011) 589–594.
- [18] G. Ribárik, J. Gubicza, T. Ungár, *Mater. Sci. Eng. A* 387–389 (2004) 343–347.
- [19] J. Gubicza, *X-ray Line Profile Analysis in Materials Science*, IGI-Global, Hershey, PA, USA, 2014.
- [20] K. Máthys, K. Nylas, A. Axt, I.C. Dragomir, T. Ungár, P. Lukáč, *Acta Mater.* 52 (2004) 2889–2894.
- [21] I.C. Dragomir, T. Ungár, *J. Appl. Crystallogr.* 35 (2002) 556–564.
- [22] R. Kuzel, P. Klimanek, *J. Appl. Crystallogr.* 21 (1988) 363–368.
- [23] M. Wilkens, in: J.A. Simmons, R. de Wit, R. Bullough (Eds.), *Theoretical Aspects of Kinematical X-ray Diffraction Profiles from Crystals Containing Dislocation Distributions*, Fundamental Aspects of Dislocation Theory, vol. II, Spec. Publ. No. 317, National Bureau of Standards, Washington, DC, USA, 1970, pp. 1195–1221.
- [24] Y. Estrin, A. Molotnikov, C.H.J. Davies, R. Lapovok, *J. Mech. Phys. Solids* 56 (2008) 1186–1202.
- [25] H. Somekawa, K. Hirai, H. Watanabe, Y. Takigawa, K. Higashi, *Mater. Sci. Eng. A* 407 (2005) 53–61.
- [26] M. Janeček, J. Čížek, J. Gubicza, J. Vrátná, *J. Mater. Sci.* 47 (2012) 7860–7869.
- [27] R.B. Figueiredo, T.G. Langdon, *Mater. Sci. Eng. A* 501 (2009) 105–114.
- [28] R.B. Figueiredo, T.G. Langdon, *J. Mater. Sci.* 44 (2009) 4758–4762.
- [29] J. Gubicza, *Defect Structure in Nanomaterials*, Woodhead, Cambridge, UK, 2012.
- [30] H.J. Frost, M.F. Ashby, *Deformation Mechanism Maps*, Pergamon Press, Oxford, 1982.
- [31] K.P. Rao, Y.V.R.K. Prasad, J. Dzwonczyk, N. Hort, K.U. Kainer, *Metals* 2 (2012) 292–312.
- [32] C. Caceres, P. Lukáč, *Philos. Mag.* 88 (2008) 977–989.
- [33] D.H. Chung, W.R. Buessem, in: F.W. Vahldiek, S.A. Mersol (Eds.), *The Elastic Anisotropy of Crystals Anisotropy in Single-Crystal Refractory Compounds*, vol. 2, Plenum Press, New York, 1968, pp. 217–245.